Research Article | Vol. 34, No. 13 / 29 Jun 2026 / Optics Express 23393
Optics EXPRESS

Full-field dual modulation fluorescence lifetime imaging on rare earth ion upconversion

YUNFAN XU,[1,*] MING FU,[1] TOBY SEVERS,[1] XIAOFEI XIAO,[1] ROSS C. SCHOFIELD,[1] STEFAN A. MAIER,[1,2] FANG XIE,[3] AND RUPERT F. OULTON[1,4]

[1]*Blackett Laboratory, Department of Physics, Imperial College London, Prince Consort Road, London, SW7 2AZ, UK*
[2]*Department of Materials, Imperial College London, Prince Consort Road, London, SW7 2AZ, UK*
[3]*Department of Physics and Astronomy, Monash University, Melbourne, 3800, Australia*
[4]*r.oulton@imperial.ac.uk*
[*]*yx3822@ic.ac.uk*

Abstract: Fluorescence lifetime imaging microscopy (FLIM) is a powerful technique to map molecular environments independently of fluorophore density and excitation intensity. Despite its success, FLIM can be slow for long-lived and weak fluorescence. Here, we introduce full-field dual modulation FLIM (FDM-FLIM) for imaging weak and long-lived emitters. By modulating the excitation and emission and projecting the signal directly onto a camera, FDM-FLIM extracts lifetimes without frequency-domain phase retrieval. We demonstrate this for Er/Yb upconversion nanoparticles near plasmonic nanostructures, where Purcell-enhanced emission leads to spatially varying lifetimes that are otherwise obscured by nanoparticle-density variations, indicating that FDM-FLIM is a robust and accessible approach for full-field and hyperspectral lifetime imaging.

Published by Optica Publishing Group under the terms of the Creative Commons Attribution 4.0 License. Further distribution of this work must maintain attribution to the author(s) and the published article's title, journal citation, and DOI.

1. Introduction

Fluorescence lifetime imaging microscopy (FLIM) is a powerful contrast approach for mapping and observing processes in biological specimens [1] as well as other physical systems [2–6]. Unlike fluorescence signal based imaging, FLIM is immune to variations in excitation intensity and fluorophore density since the lifetime is self-calibrating, enabling straightforward comparison between different samples, even on different instruments [1]. FLIM has applications in a wide range of fields due to its sensitivity to factors that influence the local molecular environment, such as temperature, pH, and ion concentration [1,7–9]. This sensitivity not only allows for the acquisition of static information, but also enables the observation of dynamic processes, such as energy transfer, through changes in the fluorescence lifetime [10–12]. Other advantages include distinguishing fluorescence markers with similar spectra and eliminating autofluorescence noise [13].

FLIM can be broadly categorized into time and frequency-domain approaches. Time-domain methods include time-correlated single photon counting (TCSPC), where photon arrival times are histogrammed after pulsed excitation and then fit to exponential decays [14,15]. Avalanche photodiodes enable fast imaging of short-lived fluorophores but the method slows for long-lived probes such as rare-earth ions [16]. Parallel detection and time-tagging schemes enable TCSPC for long lifetimes, but often entail higher system cost, demanding data handling, and system complexity. Meanwhile, wide-field camera-based time-domain approaches recover lifetimes by gating or fast switching of the detection window (e.g. using intensified, electron-muliplying or SPAD array cameras) [17–20]. In the case of frequency-domain approaches, lifetime is determined from the phase delay between modulated excitation and emission [21]. Despite its high

#599660 https://doi.org/10.1364/OE.599660
Journal © 2026 Received 31 Mar 2026; revised 5 Jun 2026; accepted 5 Jun 2026; published 16 Jun 2026

Optics EXPRESS

acquisition speed, frequency-domain FLIM requires bright signals and accurate phase-tracking electronics, again making long-lived and weakly emitting fluorophores difficult to measure [6]. Rare-earth probes challenge both methods (long lifetimes and weak fluorescence) yet offer sharp emission lines, lifetimes longer than autofluorescence, high photostability, and strong nonlinearities enabling up/down-conversion imaging [22,23].

In this paper, we report an alternative frequency-domain FLIM approach, developed for the study of rare-earth ion emission near metallic nanostructures that control their fluorescence lifetime through the Purcell effect [24–27]. Full-field Dual Modulation FLIM (FDM-FLIM) simultaneously modulates excitation and emission with a fixed π phase offset while sweeping the modulation frequency ν. This allows the camera to integrate only the fluorescence decay segment in each cycle, transforming lifetime recovery into fitting the pixel-wise amplitude–frequency response $F(\nu) = \nu\tau \tanh\left(1/(4\nu\tau)\right)$ to directly obtain full-field lifetime images. Since FDM-FLIM requires only the emission signal amplitude, weak signals, such as from rare-earth upconversion emitters, can be integrated directly on a camera [27,28]. Compared to TCSPC, which timestamps individual photons and slows as τ increases [14,15], FDM-FLIM integrates the decay half-cycle each period, maintaining signal independent of lifetime. Resolvable lifetimes are, in principle, only limited by the speed and synchronization of the dual modulation approach. The same principle naturally supports operation via imaging spectroscopy, making FDM-FLIM amenable to hyperspectral lifetime microscopy [29]. Electro-optic FLIM (EO-FLIM) is a wide-field, time-domain lifetime imaging technique that uses a Pockels cell as an optical gate [30]. The mechanical modulator, compared to the Pockels cells, does not restrict the polarization state of the signal, which is a benefit over EO-FLIM [30].

In our implementation, chopper-based dual modulation is low cost, provides high on/off contrast and field-uniform modulation, and allows full-field imaging [31]. Time-gated fluorescence imaging has long been used to measure extended lifetimes of lanthanide and phosphorescent emitters [32–34], with mechanical gating often used to reject autofluorescence [35,36]. However, delayed detection alone does not overcome the long acquisition times of time-domain decay sampling [37], nor the signal-to-noise constraints typical of frequency-domain measurements. Here, FDM-FLIM uses the same simple and inexpensive mechanical modulation to achieve rapid imaging of weak, long-lived emitters, making it well suited to rare-earth emitters with lifetimes from μs to ms.

In this study, we use FDM-FLIM to extract the lifetime of upconversion fluorescence at 660 nm (excited at 980 nm) from Er/Yb nano particles (NPs) bound to plasmonic antennas and 'ICL'-shaped gold films. Meanwhile, the binding of thiolated fluorescent particles to gold structures of vastly different scales creates large variations in particle density and lifetime. The plasmonic antennas, being sparsely distributed, ensure that these particles present far weaker fluorescence and shorter lifetime due to the Purcell effect. Particles attached to the extended gold-film regions pack more densely, producing brighter fluorescence but with a weaker Purcell effect. This sample shows FDM-FLIM's high-fidelity visualisation of spatial fluorescence lifetime contrast.

2. Materials and method

2.1. Preparation of sample

Gold nanostructures (ICL pattern and antenna gaps) were fabricated by electron-beam lithography on a cleaned 175 μm glass substrate, followed by thermal evaporation of 2 nm Cr and 50 nm Au and standard lift-off. SEM imaging was performed on a Raith e_LINE at 10.0 kV (InLens, 10 mm working distance, 30 μm aperture). Er/Yb upconversion NPs (SH-PEG1000 core–shell; Kamulin Biotech, cat. R-SUW-540; 657.9 nm emission) were incubated with the gold nanostructures in solution at 0.25 $mg\ mL^{-1}$ for 24 hours to form covalent Au–S bonds between the gold surface and thiol ligands. Full fabrication and imaging protocols are provided in the Supplement 1.

Optics EXPRESS

2.2. Fluorescence upconversion lifetime dynamics

Upon 980 nm excitation the sensitizer Yb^{3+} is resonantly driven from $^2F_{7/2}$ to $^2F_{5/2}$. Energy transfer (ET) from excited Yb^{3+} to the activator Er^{3+} proceeds in two steps (Fig. 1(c)): the first ET promotes Er^{3+} from its ground manifold $^4I_{15/2}$ (population N_g) to $^4I_{11/2}$. A subsequent ET elevates Er^{3+} to the upper manifold (population N_e). Rapid relaxation then feeds the emitting level $^4F_{9/2}$ (population N), followed by radiative decay $^4F_{9/2} \rightarrow {}^4I_{15/2}$ that yields the 657.9 nm emission (Fig. 1(d)). In the weak-excitation regime, this two-step Yb → Er energy transfer process is fast (about 170 μs [39]), and hence the emission intensity scales quadratically with the pump rate, shown in Supplement 1. The dynamics of the intermediate states can be described by:

$$\dot{N} = \gamma N_e - \Gamma N, \tag{1}$$

$$\dot{N}_e = R^2(t)(N_g - N_e) - \gamma N_e, \tag{2}$$

where the dot on N and N_e indicate the time derivative of these two parameter. γ and $\Gamma = \tau^{-1}$ are the transition and decay rates, respectively, and $R^2(t)$ is the modulated pump excitation rate, where the square indicates the quadratic scaling with pump intensity. Assuming fast relaxation from $^4F_{7/2}$, the fluorescence-relevant dynamics reduce to:

$$\dot{N} = -\frac{N}{\tau} + R^2(t)N_g, \tag{3}$$

with $\tau = \Gamma^{-1}$ is the fluorescence lifetime. Under weak (unsaturated) pump conditions, N_g is approximately the constant total population. For the modulated pump of period T, $R(t) = R_0$ for $0 \leq t < T/2$ and 0 for $T/2 \leq 0 < T$. (Setup shown in Fig. 1(a).) For the modulated emission of the same period, only the decay portion of the emission is integrated by the camera (grey area in Fig. 1 (b)). The rate equation in $N(t)$ can thus be solved to yield the emission signal $S(t) = N(t)/\tau$. Then, the integrated detected signal in the second half period $P_\pi(\nu)$ is given by:

$$P_\pi(\nu) = \eta\nu\tau t_{\text{int}} S_0 \tanh\left(\frac{1}{4\nu\tau}\right), \tag{4}$$

where η is the detection efficiency, t_{int} is the integration time, ν is the modulation frequency, and S_0 is the steady-state signal amplitude. Normalisation by the unmodulated signal, $P_* = \eta t_{\text{int}} S_0$, gives the final analytical emission (further details in Supplement 1).

$$F(\nu) = \frac{P_\pi(\nu)}{P_*} = \nu\tau \tanh\left(\frac{1}{4\nu\tau}\right). \tag{5}$$

Fitting the experimental $F(\nu)$ across modulation frequencies allows pixel-wise extraction of the fluorescence lifetime τ with high temporal sensitivity.

Unlike time domain dual modulation, like EO-FLIM, where a series of time gates are often ill-conditioned to assess multi-exponential decay [40], FDM-FLIM naturally accommodates multiple decay components. For fluorophores that exhibit multiple decay components, the FDM-FLIM model can be generalized by introducing per-pixel fractional signal contributions a_i. The corresponding ensemble-averaged ratio factor $F_a(\nu)$ is given by:

$$\frac{P_a(\nu)}{P_*} = \sum_{i=1}^{N} a_i \nu\tau_i \tanh\left(\frac{1}{4\nu\tau_i}\right), \tag{6}$$

where $\sum_i^N a_i = 1$, $a_i > 0$. This model has been applied in several lifetime measurements [24,26,27]. The Er/Yb NPs investigated here exhibit a single dominant lifetime at 657.9 *nm*. When a multi-lifetime model is applied, we find a single dominant component with τ given by the largest a_i. In practice, component identifiability depends on frequency sampling, SNR, and lifetime separation.

Optics EXPRESS

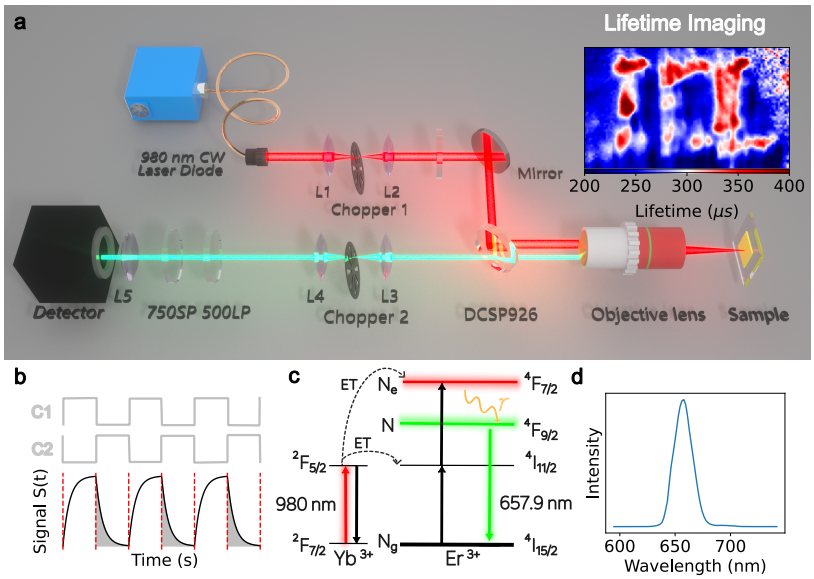


Fig. 1. (a) FDM-FLIM Schematic. An Agilent FPL4916 continuous-wave (CW) laser diode serves as the pump source. Chopper 1 (C1) modulates the pump into a square waveform and is positioned at the conjugate image plane formed by convex lenses L1 and L2 (each with $f = 10\ cm$). Chopper 2 (C2) uses the same optical configuration. A 50× Mitutoyo Plan Apo NIR Infinity Corrected Objective (NA=0.65, WD=17 mm), is used for imaging the sample. A dichroic short-pass filter divides the pump and signal (DCSP926). After further short pass filters to reduce pump light, a convex lens L5 ($f = 20\ cm$) forms the object's image on the sensor, with a magnification $M \approx \frac{f_{L5}}{f_{Objective}} \approx 11.76$. The camera used is a Teledyne Prime BSI Express (pixel size: $6.5\mu m \times 6.5\mu m$). A lifetime image of the sample is shown in the upper-right corner. (b) illustrates the modulation of the pump and detection signals. With a π phase shift of C2 relative to C1, only the grey-shaded regions are integrated by the detector [27]. (c) Schematic illustrating the electron transitions during the upconversion process, where ET indicates the energy transfer [38]. (d) Measured spectra of the signal at 657.9 nm.

3. Results and discussion

3.1. Plasmonic enhancement and lifetime contrast

To demonstrate FDM-FLIM's performance in lifetime imaging, we imaged the gold letters 'ICL' on a silica substrate (Fig. 2(c)), surrounded by plasmonic antenna gaps. The Er/Yb NP fluorescent marker is depicted in Fig. 2(c) and (d), where the core-shell structure prevents quenching [41]. During NP preparation, a thiol (SH) functional group is used to functionalize the NPs, facilitating their bonding to gold surfaces. As a result, the Er/Yb NPs are attached to both the 'ICL' gold pattern and the nano-antennas. The nano-antennas gaps are designed to enhance the local electromagnetic fields at both the excitation and emission wavelengths (shown in Fig. 2(a)). Moreover, NPs in the nano-antenna gap regions exhibit shorter fluorescence lifetimes due to plasmonic enhancement, whereas those on the 'ICL' pattern display longer lifetimes. The planarity of the 'ICL' regions is confirmed by SEM (Fig. 2(b)). Moreover, the NPs (≈ 28 nm in diameter) are substantially larger than the residual surface roughness of the nanofabricated film. Therefore, antenna-like plasmonic hot-spot effects from nanoscale asperities are negligible on the gold film. Lifetime contrast can be visualized through fluorescence lifetime imaging, with the ratio between the Purcell factor in the antenna gap $P_{F,\ AG}$ and the one in the

Optics EXPRESS

gold $P_{\mathrm{F,\,Au}}$ given by

$$\frac{P_{\mathrm{F,\,AG}}}{P_{\mathrm{F,\,Au}}} = \frac{\Gamma_{\mathrm{AG}}}{\Gamma_{\mathrm{Au}}} = \frac{\tau_{\mathrm{Au}}}{\tau_{\mathrm{AG}}} \tag{7}$$

Where Γ_{AG} and Γ_{Au} denote the fluorescence decay rates in the antenna gaps and planar gold regions, respectively. Thus, we evaluate plasmonic enhancement using the lifetime contrast defined above.

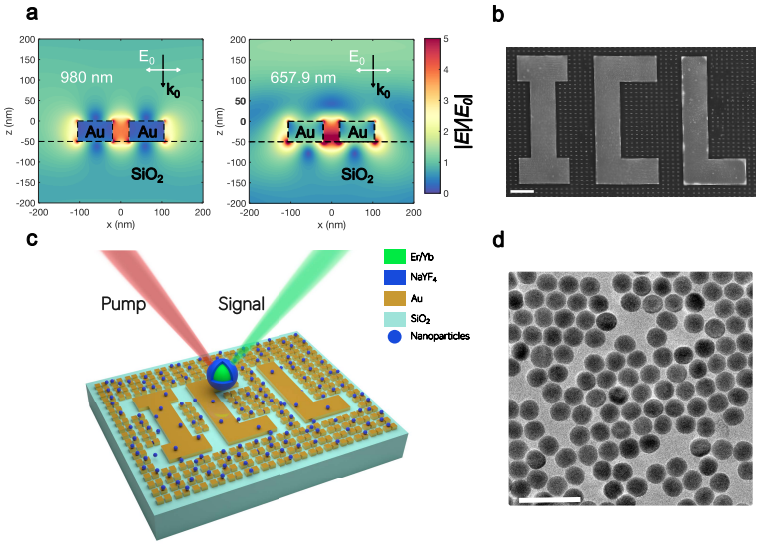


Fig. 2. (a) The simulation of Near-field distribution around the antenna gaps at the excitation wavelength (980 nm) and the signal wavelength (657.9 nm), with polarisation perpendicular to the gap. (b) SEM image of the nanogold structure (scale bar at 2 μm). (c) Schematic of the excitation of Er/Yb-doped NaYF4 core–shell UCNPs attached to the gold ICL pattern and surrounding antenna gaps. The oversized sphere is an illustrative callout of the core–shell architecture (not to scale). (d) TEM image of the nanoparticles (scale bar at 200 nm).

3.2. Data collection workflow

The data acquisition process is carried out using a custom-built full-field fluorescence microscopy system, illustrated in Fig. 1(a). The setup integrates an objective lens with a convex lens to focus the excitation beam and collect emission efficiently. The process starts by recording an unmodulated reference fluorescence image of the sample. This image is used to extract the baseline signal, P_*. Subsequently, two mechanical choppers—each with 10 blades—modulate the excitation and detection paths at frequencies ranging from 300 Hz to 900 Hz in 50 Hz increments. This frequency range is selected based on the expected upconversion lifetime of the Er/Yb NPs.

Each frame of the fluorescence image is acquired with an integration time of 1 s, much faster than time-domain methods, which typically require many hours [16]. When two mechanical choppers are synchronised to the π phase offset, the intensity of pump laser after both choppers should go down to 0. Therefore, optimising the phase offset thus involves minimising the pump laser.

3.3. Asynchronous modulation correction

Mechanical modulation leads to asynchronous modulation of different pixels, resulting in a timing displacement in the second modulation, as shown in Fig. 3(a). Pixels farther from the

Optics EXPRESS

center experience temporal shifts in modulation, causing a systematic error in $F(\nu)$. In our experimental setup, within the small excitation area, the errors on either side of the center are symmetric, opposite, and linearly proportional to the pixel's distance to the excitation center, denoted as l, as indicated in Fig. 3(b) (details in Supplement 1).

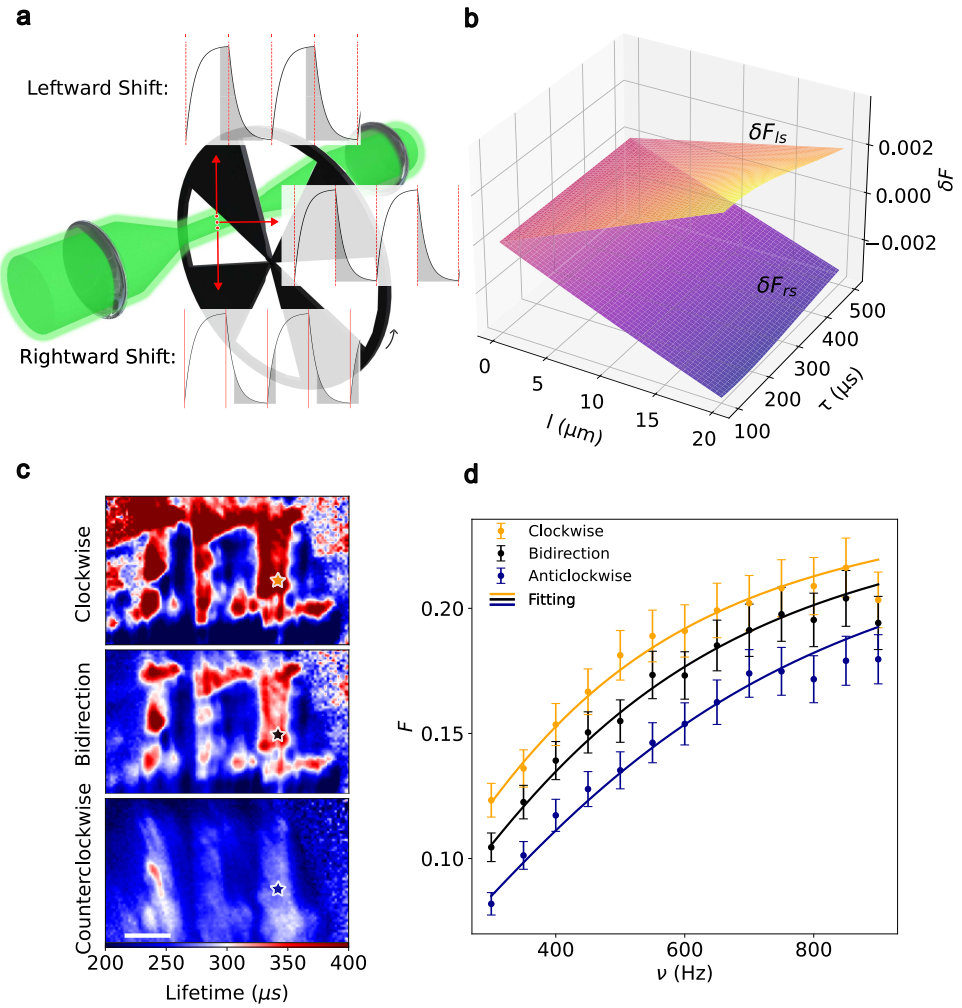


Fig. 3. (a) Schematic illustration of the shift in the second square wave caused by asynchronous modulation. The grey regions represent the actual signals detected by the camera across different pixels. (b) Three-dimensional plot of the modulation error δF as a function of deviation distance l and fluorescence lifetime τ, with a modulation frequency ν = 600 Hz. (c) The top and bottom images display the lifetime images with the second chopper rotating clockwise and counterclockwise, respectively, while the middle image shows the results under bidirectional modulation. The star in all three images highlights the pixel used to show the deviation in F caused by asynchronous modulation in (d). The scale bar is at 2 μm (d). The lifetime imaging fitting plots for the three modulation conditions in (c), illustrating the systematic error in F.

These systematic errors can be removed experimentally. First, a fluorescence image is acquired for each modulation frequency, corresponding to the modulated intensity term P_π as defined in Eq. (4). The procedure is then repeated with the second chopper rotating in the opposite

Optics EXPRESS

direction, yielding a second set of measurements for P_π. The final values of P_π are obtained by averaging the two datasets to minimize systematic errors. Pixel-wise intensity ratios $F(\nu)$ are then computed and fitted to the theoretical model, enabling the extraction of the fluorescence lifetime τ for each pixel. This bidirectional modulation approach cancels pixel-dependent timing skew. We quantify residuals and include calibration steps. Then we aggregate these lifetime results to generate a spatially resolved lifetime image. Figure 3(c) compares images obtained using bidirectional modulation with those generated by single-direction modulation, where chopper 2 rotates either clockwise or counterclockwise. Bidirectional modulation yields higher-quality lifetime maps, while the deviation in $F(\nu)$ arising from asynchronous modulation is shown in Fig. 3(d). Together, these results demonstrate the effectiveness of bidirectional modulation in reducing systematic errors.

3.4. Lifetime imaging

Multiple lifetime images are captured across fabricated 'ICL' structures. One of the fluorescence and lifetime imaging of the 'ICL' pattern are presented in Fig. 4(a) and (b). The measured lifetimes span 155 μs to 426 μs. For comparison, Er/Yb core–shell nanoparticles without plasmonic enhancement exhibit a lifetime of 474 μs [42]. The observed reduction under the gold-film and antenna-gap configuration is consistent with plasmonic Purcell enhancement, indicating that the FDM-FLIM measurements are physically credible. Moreover, presenting all FLIM maps on the same lifetime scale ensures direct comparability and strongly supports the correctness and reliability of the FDM-FLIM technique. All lifetime images reveal the shape of the 'ICL' pattern, demonstrating a significant difference in the lifetime span throughout the structure. The extensive surface area of the 'ICL' pattern leads to a significantly higher density of NPs compared to the antenna gaps regime, resulting in higher brightness in fluorescence imaging. However, the concentration of NPs does not influence the lifetime of emission [17]. The shorter lifetime observed in the antenna gaps area, as measured by FDM-FLIM, suggests the presence of stronger plasmonic enhancement by the antenna-gap structures.

In fluorescence intensity imaging, the horizontal segment of the letter 'L' is difficult to discern due to its relatively low brightness in the image. This diminished signal likely results from an insufficient number of NPs attached to that region. However, in the corresponding fluorescence lifetime imaging, the horizontal bar of the 'L' is clearly visible. This demonstrates that fluorescence lifetime is independent of fluorophore concentration [17], thereby compensating for the limitations of intensity-based imaging in such contexts. A line scan along the central axis, shown on the right side of the lifetime image, reveals variations in lifetime that correspond well with the spatial distribution of antenna gaps and gold regions. Figure 4(c) present the fitting for a pixel in the antenna gaps regions and a pixel bound to the gold 'ICL' structure, demonstrating the lifetime contrast caused by the Pucell factor difference.

The quality of the fitting is further supported by the spatial distribution of the coefficient of determination, R^2. Across and around the 'ICL' structure, R^2 values generally exceed 0.95, indicating a strong goodness-of-fit. Since the model involves fitting only a single parameter, the risk of overfitting is minimal. Moreover, We measured the lifetimes of nanoparticles on a glass substrate using both our technique and conventional TCSPC. The two measurements were in close agreement (see Supplement 1), further demonstrating the robustness of our method.

The Purcell factor ratio between the nano-antenna area and the 'ICL' gold film, which quantifies the plasmonic enhancement, is determined by comparing the lifetimes of all enhanced pixels on the antenna gaps region with those on the plain gold with R^2 over 0.95. We segment the antenna gap and gold-film regions by geometry. This analysis yields a Purcell factor ratio $P_{\mathrm{F,\,AG}}/P_{\mathrm{F,\,Au}}$ at 1.2 ± 0.2. Practically, this experimental ratio represents the structure-wide average Purcell enhancement, as it aggregates many spatially distributed measurements across distinct local environments. To benchmark against theory, we performed orientation-averaged electromagnetic

Optics EXPRESS

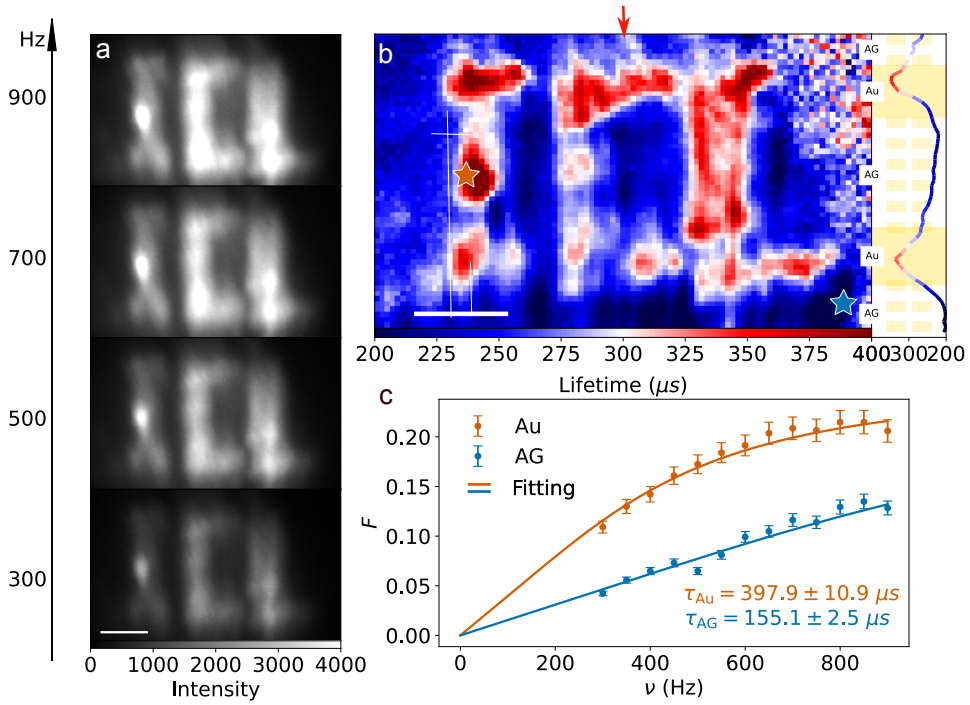


Fig. 4. (a) Fluorescence image of the 'ICL' structure under modulation, with a scale bar corresponding to 2 μm. The fluorescence intensity increases with increasing modulation frequency, consistent with the behaviour predicted by Eq. (5). (b) Lifetime image of the 'ICL' pattern, also shown with a 2 μm scale bar. A vertical line scan through the center (red arrow) is plotted at right, where Au indicates the pure gold film area and AG indicates the antenna gaps area. The lifetime peaks spatially correlate with the two gold arms forming the letter 'C'. (c) Representative lifetime fitting curves for two selected pixels located on the gold film and nano-antenna regions (marked in b). A clear contrast in lifetime values is observed between the two regions.

simulations by placing three orthogonal electric dipoles (x, y and z) at least 15 nm from the gold interface and averaging the resulting Purcell factors across these orientations. We evaluated the corresponding Purcell factor ratios at five representative positions relative to the gold-film reference (Fig. S2.1(a)), alongside the experimental measurement. Critically, the experimental ratio $P_{\mathrm{F,\,AG}}/P_{\mathrm{F,\,Au}} = 1.2 \pm 0.2$ lies within the spread of the simulated ratios. Equivalently, the measured lifetime falls within the simulated lifetime regime, which substantiates the correctness and quantitative reliability of FDM-FLIM.

To comprehensively evaluate the lifetime sensitivity of the FDM-FLIM system, we computed the minimum resolvable lifetime difference ($\delta\tau_{min}$) across the entire image. This was realised by sliding a 3×3 window over each pixel (excluding the image borders) and calculating the standard deviation of the lifetime values (σ_t) within each patch. Only regions where all pixels exhibited an $R^2 \geq 0.95$ were considered, ensuring that the analysis was restricted to areas with high-quality lifetime fits. For each valid region, $\delta\tau_{min}$ was estimated as $\tau_{min} = 2\sigma_\tau$, providing a local measure of the system's ability to distinguish small lifetime differences. This analysis revealed spatial heterogeneity in sensitivity, with minimum $\delta\tau_{min}$ values of 3.20 μs, indicating that FDM-FLIM can resolve microsecond lifetime differences.

Optics EXPRESS

4. Conclusion

We have introduced and demonstrated FDM-FLIM for lifetime imaging of Er/Yb NPs on gold nanostructures with microsecond scale time resolutions. The ICL-shaped structure is visualized through lifetime imaging, with the observed lower lifetime values in the nano-antennas' gaps regions aligning with our theoretical expectations. The Purcell factor ratio $P_{\mathrm{F,\,AG}}/P_{\mathrm{F,\,Au}}$, measured at 1.2 ± 0.2, was determined using FDM-FLIM, highlighting its potential to investigate surface-enhanced light matter interactions. Furthermore, the minimum resolvable lifetime difference, $\delta\tau_{\mathrm{min}}$, was quantified to be 3.20 μs, demonstrating the technique's high sensitivity in resolving microsecond-level lifetime variations. This level of precision is advantageous for imaging lanthanide-based probes, and shows the potential of the method for enabling the development of novel fluorescence markers in emerging application areas. Moreover, the detectable lifetime range of FDM-FLIM is primarily influenced by the modulation frequency, so with faster modulation approaches, we could extend this range to the nanoseconds scale. With flexibility to vary the integration time, the technique is capable of FLIM with extremely weak signals. Where signals are stronger, rapid full-field lifetime acquisition via FDM-FLIM suggests application to medical imaging. Additionally, the cost-effectiveness of FDM-FLIM suggests an accessible option for research laboratorys. The straightforward setup and calibration of FDM-FLIM facilitate its possible integration with superresolution technologies, such as STED.

Funding. Leverhulme Trust (RPG-2016-064).

Acknowledgment. We gratefully acknowledge financial support from CPLAS Grant, RPLAS Grant, the Leverhulme Trust (grant RPG-2016-064).

Disclosures. The authors declare no conflicts of interest.

Data availability. Data underlying the results presented in this paper are not publicly available at this time but may be obtained from the authors upon reasonable request.

Supplemental document. See Supplement 1 for supporting content.

References

1. R. Datta, T. M. Heaster, J. T. Sharick, *et al.*, "Fluorescence lifetime imaging microscopy: fundamentals and advances in instrumentation, analysis, and applications," J. Biomed. Opt. **25**(07), 1–071203 (2020).
2. H. Vu, J. W. Woodcock, A. Krishnamurthy, *et al.*, "Visualization of polymer dynamics in cellulose nanocrystal matrices using fluorescence lifetime measurements," ACS Appl. Mater. Interfaces **14**(8), 10793–10804 (2022).
3. M. Wohlschläger, M. Versen, M. G. Löder, *et al.*, "Identification of different plastic types and natural materials from terrestrial environments using fluorescence lifetime imaging microscopy," Anal. Bioanal. Chem. **416**(15), 3543–3554 (2024).
4. N. Lee, D. Afanasenkau, P. Rinklin, *et al.*, "Temperature profile characterization with fluorescence lifetime imaging microscopy in a thermophoretic chip," Eur. Phys. J. E **44**(10), 130 (2021).
5. S. A. Schulz, R. Oulton, M. Kenney, *et al.*, "Roadmap on photonic metasurfaces," Appl. Phys. Lett. **124**(26), 260701 (2024).
6. X. Liu, A. Skripka, Y. Lai, *et al.*, "Fast wide-field upconversion luminescence lifetime thermometry enabled by single-shot compressed ultrahigh-speed imaging," Nat. Commun. **12**(1), 6401 (2021).
7. S. Ogikubo, T. Nakabayashi, T. Adachi, *et al.*, "Intracellular ph sensing using autofluorescence lifetime microscopy," J. Phys. Chem. B **115**(34), 10385–10390 (2011).
8. K. Okabe, N. Inada, C. Gota, *et al.*, "Intracellular temperature mapping with a fluorescent polymeric thermometer and fluorescence lifetime imaging microscopy," Nat. Commun. **3**(1), 705 (2012).
9. X.-M. Cai, S. Li, W.-J. Wang, *et al.*, "Natural acceptor of coumarin-isomerized red-emissive bioaiegen for monitoring cu2+ concentration in live cells via flim," Adv. Sci. **11**(9), 2307078 (2024).
10. W. Becker and A. Bergmann, "Lifetime imaging techniques for optical microscopy," Tech-nical report, Becker & Hickl GmbH (2003).
11. M. Hedayati, Y.-I. Chen, J. R. Houser, *et al.*, "Visualizing molecular deformation in fibrin networks under tensile loading via flim–fret," Chem. Commun. **59**(98), 14575–14578 (2023).
12. T. Spatola Rossi, C. Pain, S. W. Botchway, *et al.*, "Fret-flim to determine protein interactions and membrane topology of enzyme complexes," Current Protocols **2**(10), e598 (2022).
13. K. Koenig, U. Wollina, I. Riemann, *et al.*, "Optical tomography of human skin with subcellular spatial and picosecond time resolution using intense near infrared femtosecond laser pulses," in *Multiphoton Microscopy in the Biomedical Sciences II*, vol. 4620 (SPIE, 2002), pp. 191–201.

Optics EXPRESS

14. D. Phillips, R. Drake, D. O'Connor, *et al.*, "Time correlated single-photon counting (tcspc) using laser excitation," Instrum. Sci. Technol. **14**(3-4), 267–292 (1985).
15. W. Becker, A. Bergmann, and C. Biskup, "Multispectral fluorescence lifetime imaging by tcspc," Microsc. Res. Tech. **70**(5), 403–409 (2007).
16. D. Cano, A. Ferrier, K. Soundarapandian, *et al.*, "Fast electrical modulation of strong near-field interactions between erbium emitters and graphene," Nat. Commun. **11**(1), 4094 (2020).
17. W. Becker, "Fluorescence lifetime imaging–techniques and applications," J. Microsc. **247**(2), 119–136 (2012).
18. J. McGinty, J. Requejo-Isidro, I. Munro, *et al.*, "Signal-to-noise characterization of time-gated intensifiers used for wide-field time-domain flim," J. Phys. D: Appl. Phys. **42**(13), 135103 (2009).
19. J. Bosiers, H. van Kuijk, W. Klaassens, *et al.*, "Mem-flim, a ccd imager for fluorescence lifetime imaging microscopy," in *Proc. Int. Image Sensor Workshop (IISW)*, (2013), pp. 53–56.
20. A. C. Ulku, C. Bruschini, I. M. Antolović, *et al.*, "A 512× 512 spad image sensor with integrated gating for widefield flim," IEEE J. Sel. Top. Quantum Electron. **25**(1), 1–12 (2018).
21. J. Demas, *Excited state lifetime measurements* (Elsevier, 2012).
22. J. Zhou, Y. Sun, X. Du, *et al.*, "Dual-modality in vivo imaging using rare-earth nanocrystals with near-infrared to near-infrared (nir-to-nir) upconversion luminescence and magnetic resonance properties," Biomaterials **31**(12), 3287–3295 (2010).
23. Y. Zhong and H. Dai, "A mini-review on rare-earth down-conversion nanoparticles for nir-ii imaging of biological systems," Nano Res. **13**(5), 1281–1294 (2020).
24. J. Xu, M. Fu, Y. Lu, *et al.*, "Remarkable plasmonic enhanced luminescence of ce3+ doped lanthanide downconversion nanoparticles in nir-ii window by silver hole-cap nanoarrays," Adv. Opt. Mater. **12**(30), 2400660 (2024).
25. J. Xu, M. Fu, C. Ji, *et al.*, "Plasmonic-enhanced nir-ii downconversion fluorescence beyond 1500 nm from core–shell–shell lanthanide nanoparticles," Adv. Opt. Mater. **11**(19), 2300477 (2023).
26. J. Xu, F. Ming, Y. Xu, *et al.*, "Boosting nir-i luminescence of lanthanide nanoparticles excited in nir-ii by plasmonic arrays," SSRN (2025).
27. N. A. Güsken, M. Fu, M. Zapf, *et al.*, "Emission enhancement of erbium in a reverse nanofocusing waveguide," Nat. Commun. **14**(1), 2719 (2023).
28. D. Sumetsky, J. Y. Jiang, M. A. Ayad, *et al.*, "Linear behavior of the phase lifetime in frequency-domain fluorescence lifetime imaging of fret constructs," Front. Phys. **9**, 648016 (2021).
29. R. A. Schultz, T. Nielsen, J. R. Zavaleta, *et al.*, "Hyperspectral imaging: a novel approach for microscopic analysis," Cytometry **43**(4), 239–247 (2001).
30. A. J. Bowman, C. Huang, M. J. Schnitzer, *et al.*, "Wide-field fluorescence lifetime imaging of neuron spiking and subthreshold activity in vivo," Science **380**(6651), 1270–1275 (2023).
31. C. M. McGraw, G. Khalil, and J. B. Callis, "Comparison of time and frequency domain methods for luminescence lifetime measurements," J. Phys. Chem. C **112**(21), 8079–8084 (2008).
32. V. Y. Soloviev, K. B. Tahir, J. McGinty, *et al.*, "Fluorescence lifetime imaging by using time-gated data acquisition," Appl. Opt. **46**(30), 7384–7391 (2007).
33. V. Buschmann, S. Orthaus, A. Devaux, *et al.*, "Phosphorescence lifetime imaging microscopy (plim) measurements: Practical aspects," *PicoQuant Technical Note, Ic* pp. 1–10 (2016).
34. W. Yang and S.-L. Chen, "Time-gated fluorescence imaging: Advances in technology and biological applications," J. Innovative Opt. Health Sci. **13**(03), 2030006 (2020).
35. R. Connally, "A device for gated autosynchronous luminescence detection," Anal. Chem. **83**(12), 4782–4787 (2011).
36. S. S. Kanani, H.-Y. Tsai, and W. R. Algar, "Quantitative and multiplexed chopper-based time-gated imaging for bioanalysis on a smartphone," Anal. Chem. **95**(35), 13258–13265 (2023).
37. G. Marriott, R. M. Clegg, D. J. Arndt-Jovin, *et al.*, "Time resolved imaging microscopy. phosphorescence and delayed fluorescence imaging," Biophys. J. **60**(6), 1374–1387 (1991).
38. Y. Wang, G. Sun, Q. Su, *et al.*, "Optical upconversion in mononuclear lanthanide co-crystal assemblies," Chemistry A European J. **30**(35), e202400911 (2024).
39. D. Lu, C. Mao, S. K. Cho, *et al.*, "Experimental demonstration of plasmon enhanced energy transfer rate in nayf4: Yb3+, er3+ upconversion nanoparticles," Sci. Rep. **6**(1), 18894 (2016).
40. N. Ronceray, S. Bennani, M. F. Mitsioni, *et al.*, "Wide-field fluorescence lifetime imaging of single molecules with a gated single-photon camera," Light: Sci. Appl. **14**(1), 258 (2025).
41. N. J. Johnson, A. Korinek, C. Dong, *et al.*, "Self-focusing by ostwald ripening: a strategy for layer-by-layer epitaxial growth on upconverting nanocrystals," J. Am. Chem. Soc. **134**(27), 11068–11071 (2012).
42. L. T. K. Giang, K. Trejgis, L. Marciniak, *et al.*, "Fabrication and characterization of up-converting β-nayf4: Er3+, yb3+@ nayf4 core–shell nanoparticles for temperature sensing applications," Sci. Rep. **10**(1), 14672 (2020).